











Opto-thermally controlled beam steering in nonlinear all-dielectric metastructures

DAVIDE ROCCO,^{1,2,*}  MARCO GANDOLFI,^{1,2}  ANDREA TOGNAZZI,^{1,2}  OLESIYA PASHINA,³ GEORGE ZOGRAF,³ KRISTINA FRIZYUK,³  CARLO GIGLI,⁴  GIUSEPPE LEO,⁴  SERGEY MAKAROV,³ MIHAIL PETROV,³  AND COSTANTINO DE ANGELIS^{1,2,3} 

¹Department of Information Engineering, University of Brescia, via Branze 38, 25123 Brescia, Italy

²CNR-INO (National Institute of Optics), via Branze 45, 25123 Brescia, Italy

³ITMO University, Department of Physics and Engineering, St. Petersburg, Russia

⁴Matériaux et Phénomènes Quantiques, Université de Paris & CNRS, 75013 Paris, France

*davide.rocco@unibs.it

Abstract: Reconfigurable metasurfaces have recently gained a lot of attention in applications such as adaptive meta-lenses, hyperspectral imaging and optical modulation. This kind of metastructure can be obtained by an external control signal, enabling us to dynamically manipulate the electromagnetic radiation. Here, we theoretically propose an AlGaAs device to control the second harmonic generation (SHG) emission at nanoscale upon optimized optical heating. The asymmetric shape of the used meta-atom is selected to guarantee a predominant second harmonic (SH) emission towards the normal direction. The proposed structure is concurrently excited by a pump beam at a fundamental wavelength of 1540 nm and by a continuous wave (CW) control signal above the semiconductor band gap. The optical tuning is achieved by a selective optimization of meta-atoms SH phase, which is modulated by the control signal intensity. We numerically demonstrate that the heating induced in the meta-atoms by the CW pump can be used to dynamically tune the device properties. In particular, we theoretically demonstrate a SH beam steering of 8° with respect to the vertical axis for an optimized device with average temperature increase even below 90° C.

© 2021 Optical Society of America under the terms of the [OSA Open Access Publishing Agreement](#)

1. Introduction

Optical metasurfaces are 2D arrays of subwavelength resonators devised to control properties of light ranging from its wavefront to polarization and intensity distribution or spectrum. The subwavelength scatterers, also called meta-atoms, capture and re-emit the incident light [1–9]. An appropriate choice of meta-atoms geometry and mutual distance leads to an optimized modification of the characteristics of light scattered by the 2D array. Thus, metasurfaces are attractive solutions to miniaturize bulk devices such as lenses, mirrors, holograms, waveplates, polarizers, and spectral filters [10–15]. Recently, in order to extend such functionalities and implement new operations, optical metasurfaces for the control of higher harmonic emitted fields have started to gain a great deal of attention [16]. In particular, the high second order nonlinearities of the III-V semiconductors such as GaAs or AlGaAs have strongly motivated the development of nonlinear nanophotonics based on second harmonic generation (SHG) [17–22]. However, static metasurfaces present some restrictions for a realistic device. Recently, many efforts have been spent to achieve reconfigurable metasurfaces by locally tuning individual meta-atoms inside the device [23–29]. Apart from mechanical movement of elements, several approaches including anisotropic substance insertion, phase-changing materials and photo-excitation of free carriers, have been implemented. For instance, Liquid Crystal (LC) infiltration has been

exploited in [30] where the authors present an experimental study of the emission properties of fishnet metamaterials infiltrated with nematic LCs, demonstrating that moderate laser powers can be translated in valuable changes of the optical transmission of the composite structures; in [31] the LCs are used to achieve a switching between electric and magnetic resonances of a metasurface in the presence of a bias electric field to change the LC axis orientation. A similar concept, applied to the harmonic generated signal from dielectric metasurface, has been theoretically proposed in [32] where the re-orientation of the LC state can modulate not only the SH power but also the emitted SH radiation properties. Recently, it has been also proposed a hybrid approach in which the reconfigurable and multilevel control is achieved by embedding subwavelength inclusions of a switchable and tunable phase-change layer within the body of high-index all-dielectric nanoantennas. In this way, switchable spectral filters in the near-infrared and dynamic color generation in the visible spectrum have been designed [33]. Moreover, ultrafast photoinjection of dense electron-hole plasma within dielectric Mie-resonant nanoparticles has been reported in [34], where it has been shown that a femtosecond laser pump remarkably changes the transient dielectric permittivity. This permits the modification of both electric and magnetic nano-structure responses, resulting in considerable changes of its scattering efficiency. The possibility to thermally tune the metasurface behaviour has also been proposed in the linear regime owing to efficient optical heating of single all-dielectric nanoantennas [35,36]. For instance, reconfigurable metasurfaces exploiting the thermally driven insulator-to-metal phase transition of vanadium dioxide [37] and the dynamical reversible tuning of all-dielectric metasurfaces based on temperature-dependent refractive index changes in silicon have been reported [38,39]. However, the modulation of the harmonic generated signal by means of thermally controllable metastructures is still an open issue.

Here, we propose a novel approach to overcome this gap by utilizing a thermally tunable dielectric metastructure for modulating the SH signal. We base our analysis on a "nano-chair" shaped AlGaAs symmetry broken meta-unit, obtained by removing one quarter of the volume from a nanocylinder [40]. The proposed geometry bears great interest for technological applications, because it is able to focus the second harmonic signal along the cylindrical axis. Conversely from a symmetric AlGaAs nanoantenna, that implicitly presents a SH null in the forward and backward directions when the pump is impinging at normal-incidence, the nano-chair geometry guarantees a maximum of SH signal in the normal direction, even for the easily-fabricable (100) AlGaAs axis orientation [40]. The symmetry broken structure guarantees an enhancement of more than two orders of magnitude in the SH generation in a small numerical aperture ($NA = 0.1$) around the normal direction with respect to its symmetrical counterpart structure. Differently from recent works based on tunable control of the linear directional scattering from asymmetric dielectric platforms [41–43], our purpose is to achieve a detectable modulation in the SH signal. To reach this goal, the proposed metastructure is simultaneously excited by a fundamental wavelength (FW) beam in the infrared region and by a continuous wave (CW) control signal in the visible part of the spectrum. By varying the CW light intensity, I_0 , it is possible to modulate in a non-uniform fashion the temperature reached inside the dielectrics. This non trivial thermal change leads to conspicuous variations of the refractive index at the SH. Indeed, for AlGaAs the thermo-optic coefficient is of the order of 10^{-3} [r.i.u./K] for the considered wavelength range [44]. The obtained refractive index variations are associated to the tuning of the linear resonant response and consequently to detectable changes in the SH signal. Hence, we show that it is possible to create a look-up table for the emitted SH magnitude and phase as a function of I_0 . Finally, we demonstrate how to use the calculated SH emission from the meta-atoms at different I_0 to optimize a tunable structure, paving the way to thermo-optical nonlinear beam steering control.

2. Results and discussion

2.1. CW optimization

Firstly, let us consider a single isolated nano-chair as a reference structure. The asymmetric shape is the one suggested in Refs. [40,45] and it is displayed in the inset of Fig. 1(a). We consider an AlGaAs meta-unit with an elliptical base with semi-axes $r_a = 260$ nm, $r_b = 200$ nm and height $h = 400$ nm and placed over a sapphire substrate. The refractive index of the nano-chair is taken from Ref. [46] whereas the substrate permittivity is selected as in Ref. [47]. To reproduce the thermal and optical behavior of the meta-atom, we perform Finite Element Method simulations in COMSOL Multiphysics. The geometrical parameters of the nano-chair are selected to fulfill scattering resonances around the FW and the SH wavelength together with a maximum of absorption in the CW range, see Fig. 1(a). The complete fabrication procedure of a similar asymmetric geometry is described in Ref. [45]. The proposed theoretical analysis does not take into account a few nm layer at the bottom of the nano-chair that can result from the manufacturing process of such a structure but, as reported in [45], this impurity can be neglected without loss of generality.

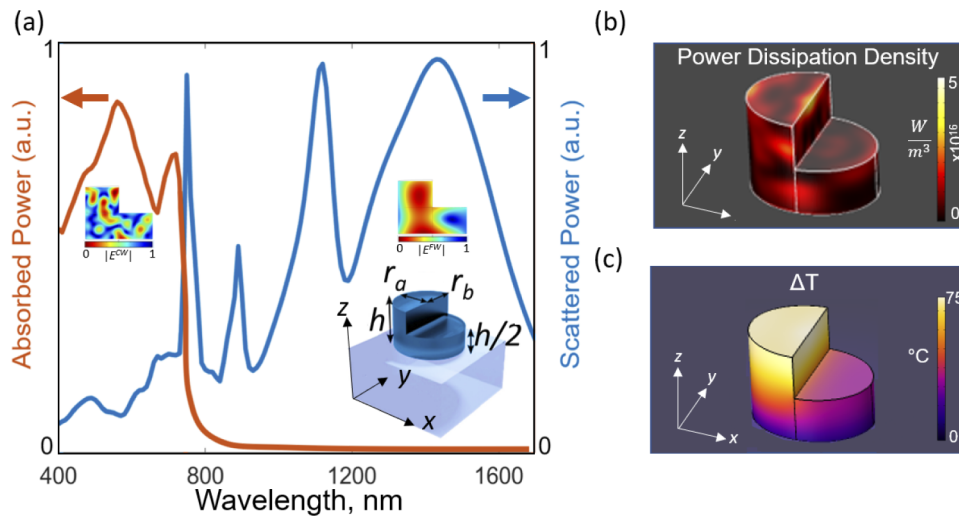


Fig. 1. (a) The scattered and absorbed powers as a function of the incident wavelength for the optimized nano-chair. The upper insets show the electric field norm at the CW and FW (xz plane), respectively. The lower inset represents a sketch of the proposed meta-unit. (b) The associated power dissipation per unit volume at $\lambda = 550$ nm, $I_0 = 200$ kW/cm². (c) Map of the temperature increase distribution, ΔT , for $\lambda = 550$ nm, $I_0 = 200$ kW/cm².

As already anticipated, the idea of this manuscript is to control the SH emission coming from the nano-chair by an external stimulus, the latter being a CW control beam in the AlGaAs absorption region (i.e. below 700 nm). We model the CW control signal as a normally incident plane wave, linearly polarized along the y axis in the wavelength range from 400 nm to 1600 nm. We solve the optical problem and calculate the absorbed power in the AlGaAs structure, the latter acting as a source term for the thermal simulation [48]. We perform a parametric sweep as a function of the incident wavelength. Although we expect that the dissipative losses are higher below 700 nm, we perform simulation in the extended range 400 nm - 1600 nm in order to highlight the extinction properties of the selected nano-chair. Indeed for wavelength greater than 700 nm the extinction is dominated by the scattering contribution while for shorter wavelength by the absorption one. The wavelength that maximize the dissipation, and accordingly the temperature enhancement within the structure, is around 550 nm, as reported in Fig. 1(a). At

550 nm we reveal a peak in the absorption spectrum of the meta-atom and the associated power dissipation density is shown in Fig. 1(b). As can be seen from Fig. 1 the power dissipation is mainly concentrated in the upper part of the nano-chair. We have estimated that an uncertainty of 10 K regarding the temperature reached inside the nano-chair is related to a fluctuation of about 30 KW/cm² in the pump intensity which is far to be small. Furthermore, Al_{0.18}Ga_{0.82}As and sapphire have high thermal conductivities, around 15 and 30 W/(m·K), respectively. The latter evidences imply that the heat diffusion towards the substrate reduces significantly the temperature in the lower part of the nano-chair, the maximum temperature increase occurring in the top of the nano-object, see Fig. 1(c). Moreover, we estimate a transition period, that is the time necessary to reach the steady-state temperature after the CW pump is turned on or off, roughly around 100 ns.

In order to estimate the dynamic of the proposed device, we perform time dependent simulations in Comsol Multiphysics. We simulate a control CW signal with intensity equal to 200 kW/cm² that is used to excite a nano-chair. The associated average steady-state temperature increase in the structure under test is equal to 46° C. We assume that the CW is turned on at the time $t_{on} = 10^{-12}$ s and we study the temperature enhancement in the AlGaAs nano-chair as a function of time, as reported in Fig. 2. Concerning the heating process, see Fig. 2, it is clear that the steady-state temperature is reached after 100 ns from t_{on} . Regarding the cooling case, that is reported in Fig. 2(b), the CW pump is instead assumed to be switched off at the time $t_{off} = 10^{-12}$ s. Again, we can notice that the time to reach the T_0 temperature is roughly 100 ns for either for the cooling process as well.

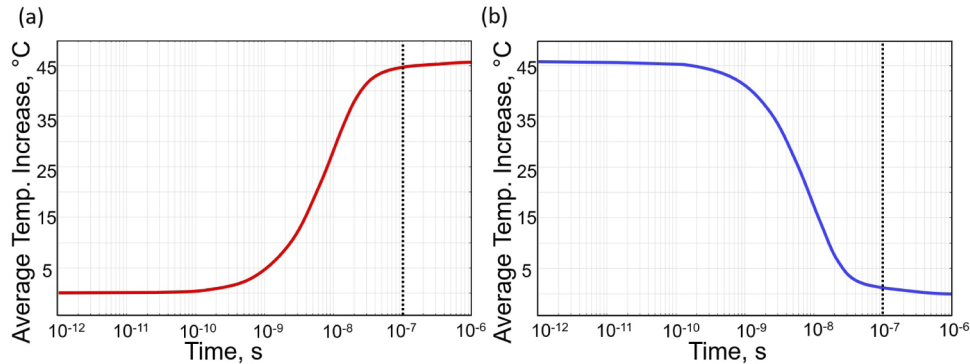


Fig. 2. (a) The heating and (b) the cooling process in terms of average temperature increase as a function of time for a nano-chair with $r_a=260$ and $r_b=200$ nm and $h=400$ nm. The black dashed line indicates the time for which the temperature reaches a value less than 1 °C from the steady-state value.

2.2. Thermo-optical problem and SHG look-up table

Now, let us assume that the nano-chair is simultaneously excited by a FW pump at 1540 nm and by the CW laser at 550 nm (chosen to optimize the light to heat conversion). The effects of the CW is to increase the temperature in the structure, the latter modifying the refractive index felt by the FW and the SH. We model the thermal dependence of the meta-atom refractive index as $n(T, \lambda, \mathbf{r}) = n(T_0) + \alpha(\lambda)[T(\mathbf{r}) - T_0]$ where n is AlGaAs refractive index and T the temperature reached in the dielectric structure at the position \mathbf{r} after the excitation with the CW pump (T_0 being the environment temperature). The coefficient α is the thermo-optic coefficient. Following the same approach reported in [44], we estimate that around 770 nm (i.e. at the SH wavelength) the coefficient α is about $4 \cdot 10^{-3}$ [r.i.u./K] while α is much smaller at 1540 nm ($\approx 10^{-4}$). Thus, in a first approximation, we neglect the refractive index variation at the FW [49]. The fundamental wavelength beam is a plane wave coming from the air region with k -vector

towards the $-z$ direction and linearly polarized along the y axis with a pump intensity equal to 1 GW/cm^2 . This value is chosen to mimic the peak intensity of a typical femto-second laser pulse. The SHG phenomena is modeled by using the nonlinear polarization induced by the nonlinear susceptibility of the second order, $\chi^{(2)}$, the latter assuming a value of 200 pm/V [40]. To be more explicit, the AlGaAs refractive index is equal to 3.27 at the FW, 3.55 at the SH and $3.94 + j0.24$ at the CW. Instead, the sapphire index is assumed to be 1.74, 1.76, 1.772 at the three corresponding wavelengths. The choice of the pump polarization is justified in the [Appendix](#). The presence of the CW beam is accounted in the computations of the SHG light, since we used the temperature dependent refractive index $n(T)$. The latter consideration is the base for the tuning of the SHG signal. As pointed out before, the temperature increase mostly affects the refractive index at the SH, since at the fundamental wavelength, $\alpha(\lambda=1540 \text{ nm}) \approx 0$. The obtained nonlinear calculations show that, for the considered CW intensity range, the SH is mainly emitted in the vertical direction towards the substrate (in other words, the radiation diagram has a main lobe along the negative z axis) and it is mainly y -polarized. In the nonlinear simulation we do not consider the effect of Two Photons Absorption [50] since AlGaAs allows TPA-free operation around the third communication window for the selected aluminum fraction ($x = 0.18$) and we also neglect the inhomogeneous broadening that may affects the dynamics of nonlinear generation. Fig. 3(a) quantifies the modification in the transmitted SH main lobe as a function of the CW power intensity, I_0 . Notably, for I_0 between 75 and 375 kW/cm^2 the emitted SH module (calculated along the vertical direction, $-z$ axis, in the far-field) is roughly constant while the SH phase at the same coordinate shows a 2 rad phase shift. Thus, the nonlinear SH mode induced in the nano-chair is engineered to control the electric field phase in the far-field while preserving a central emission lobe, see Fig. 3(b). The variations of the SH fields within the nano-chair as a function of different I_0 are reported in Fig. 3(c). The SHG efficiency of the designed structure is of the order of 10^{-6} W^{-1} . The presence of the SH main lobe in the z -direction can be explained by symmetry considerations concerning the nano-chair geometrical shape. Indeed, the second-harmonic radiation pattern strongly depends on the nanoparticle symmetry. For example, cylinder or cubic AlGaAs particles can not generate second harmonic in the upper direction under normally incident plane wave excitation (when considering canonical crystalline axis orientation) [51]. It is true that a symmetric structure has a thermal response that is very similar to the one of the nano-chair, see Fig. 4. However, the SH signal emitted by the symmetric AlGaAs nanoantenna with similar geometrical dimensions, is mostly emitted at large angles with respect to the normal, as depicted in Fig. 4(b). Instead, the chair-like particle has only one symmetry plane, thus, its symmetry group is C_2 . In such a particle, there are only two types of modes - one is even under reflection in the symmetry plane and the second one is odd [52]. Under plane wave excitation, only odd mode is excited in second harmonic. This is also confirmed by the fact that the SH main lobe is mostly y -polarized. This means, however, that all possible odd multipoles are also excited, including multipoles with $m = 1$, which give intensity contribution along the z -axis.

2.3. Nonlinear reconfigurable device

In this section, we reveal how the demonstrated variation of the SH emission of the isolated meta-atom [Fig. 3(a)] can be used to design a reconfigurable device. Let us consider 4 nano-chairs (aligned along the x direction) subject to a CW excitation in the intensity range 75 kW/cm^2 to 375 kW/cm^2 so as to guarantee a SH phase emission equally distributed in the range $[-0.4 \text{ rad}, 1.6 \text{ rad}]$ but rather constant field amplitude, see Fig. 5(a). This is experimentally possible by using an amplitude mask to calibrate the incident excitation. Moreover, for the aforementioned intensity range, the SH emission pattern maintains a main lobe y -polarized in the vertical direction with a small amplitude variation. If we assume that the SH emission from the 4 meta-atoms can be considered identical, the supercell of 4 resonators can be modeled as a broadside array of

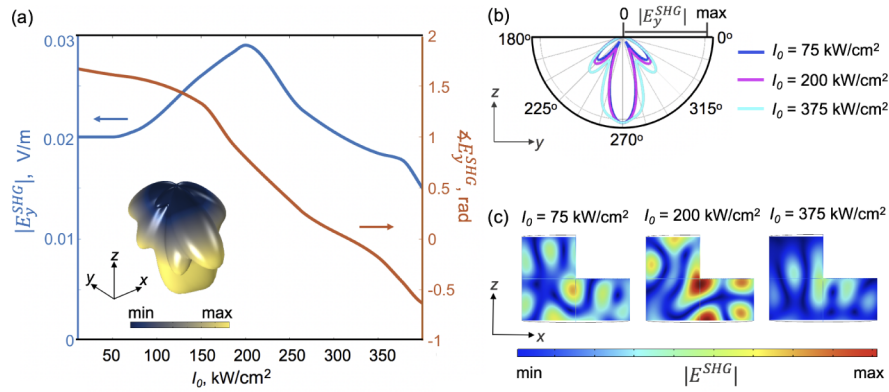


Fig. 3. (a) SH Electric field (y-component) module, $|E_y^{SHG}|$, (left axis, blue curve) and phase, $\angle E_y^{SHG}$, (right axis, orange curve) as functions of the CW irradiance. The fields are calculated along the normal direction in the Far-Field. The inset represents the total SH far-field emission for $I_0 = 200 \text{ kW/cm}^2$. (b) The normalized radiation diagram of the SH electric field (y component) for different CW intensities. The main transmitted lobe is displayed. (c) Side view of the SH electric field norm within the nano-chair for I_0 ranging from 75 to 375 kW/cm^2 .

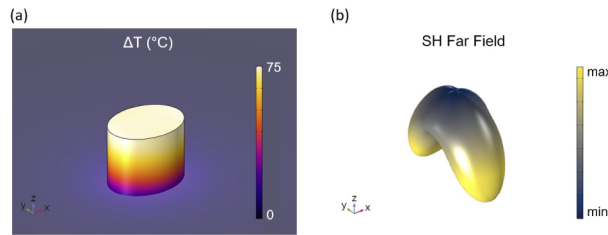


Fig. 4. (a) Map of the temperature distribution of the symmetric counterpart antenna with $r_a = 260 \text{ nm}$, $r_b = 200 \text{ nm}$ and $h = 400 \text{ nm}$ for CW pump at $\lambda = 550 \text{ nm}$, incident irradiance I_0 equal to 200 kW/cm^2 . (b) The associated SH far-field emission.

antennas. In this framework, the total SH far-field emitted from the device can be calculated by multiplying the far-field of the isolated pillar with the function known as array factor [53]. By doing this, we fix the period P of the array of antennas to the value of $0.9 \mu\text{m}$ in order to guarantee negligible inter-particle coupling [45]. Noteworthy, for the chosen lattice period, the metastructure is in the sub-diffraction regime at the FW and in the diffraction regime at the SH wavelengths. The obtained SH emission pattern of the 4 meta-units supercell ($P = 0.9 \mu\text{m}$) corresponds to the gray curve of Fig. 5(b) when considering a heating process with increasing I_0 from left to right (positive SH phase shift between the meta-units). For comparison, the SH emission of the metasurface when considering a negative SH phase shift (I_0 increasing from right to left) is represented by the magenta curve. For the designed metasurface, a SH steering angle, γ , up to 8° with a main-lobe Full-Width-Half-Maximum of about 11° has been obtained. Thus, the external thermal tuning can be translated into a dynamical tailoring of the SH emission with a tuning frequency up to 10 MHz.

We stress that in our manuscript, the following thermal effects have been neglected: (i) the presence of a thermal boundary resistance at the interface nanochair-substrate; (ii) the thermal conductivity reduction in sapphire substrate due to imperfections, as reported in [54]; (iii) the ballistic heat transport in the nano-chair, yielding a reduced thermal conductivity with respect

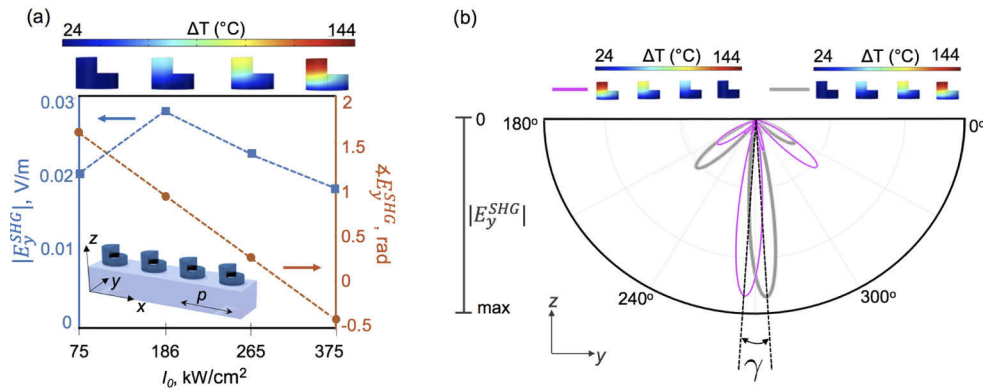


Fig. 5. (a) The amplitude (left axis, blue curve) and phase (right axis, red curve) of the SH electric field (y-component) for the selected 4 nano-chairs, as functions of I_0 . Top: map of the temperature enhancement in each meta-unit. (b) The radiation diagrams for the array SH emission (y-component) transmitted in the substrate. The gray (magenta) curve corresponds to the optimized metasurface with increasing I_0 from left to right (from right to left).

to bulk AlGaAs due to small size of the nanochair, the latter falling shorter with respect to the mean free path of a fraction of the phonons involved in the thermal transport [55,56]. Indeed, the quantitative treatment of the latter phenomena is challenging, since the precise numbers to be used are not known, potentially varying over nominally identical samples due to imperfections and depending on the particular deposition technique. Therefore, their inclusion into the modelling would increase the complexity of the interpretation of the obtained results. Anyway, we pinpoint that the inclusion of all these thermal effects would increase the temperature within the nanochair at constant CW light intensity, thus improving the tuning capability. Moreover, the heat transfer between one nano-chair to the other is very small and can be considered negligible. To prove this, we have simulated a dimer configuration in which the dielectric structures are placed at a distance $P = 0.9 \mu\text{m}$ (the one used in the supercell) and they are excited with a CW pump at a wavelength of 550 nm. To prove our ansatz, in the thermal simulation, the heat source is active in only one nano-chair of the dimer. The obtained results are shown in Fig. 6(a). The temperature increase value and distribution of the CW pump-heated nano-chair are the same as the case of isolated structure, see Figs. 6(a) and (b) for comparison. Moreover, this thermal simulation demonstrates a negligible heat transfer between the dielectrics because the temperature increase in the nano-chair without heat source is less than 4 °C, as depicted in Fig. 6(c). Hence, the results reported in this manuscript can be considered as a safe underestimate for the actual scenario.

Indeed, the choice of the periodicity implies a compromise between the requirement of optically uncoupled nanoantennas and a sub-wavelength sampling distance. To be more explicit, the geometrical size and optical coupling are the most impacting limitations. By increasing the number of resonators that form the supercell, the main lobe aperture can be reduced but at the same time the steering angle becomes smaller and smaller. The same consideration holds by increasing the period. More design details are reported in the Appendix. Please note that the proposed structure consists of 4 aligned nano-chairs along the x-axis and not in a square lattice configuration. The ability to dynamically tune the nonlinear radiation, as shown by the proposed super-cell, paves the way to optical gating of second-order nonlinear processes, enabling platforms such as ultrafast optical modulators, SH lenses and holographic metasurfaces.

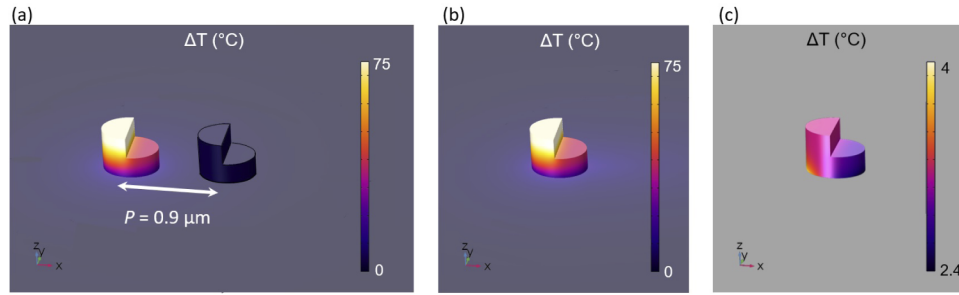


Fig. 6. (a) Temperature increase distribution for a dimer system composed of two identical nano-chairs ($r_a=260$ nm, $r_b=200$ nm, $h=400$ nm) at a distance $P = 0.9 \mu\text{m}$ from each other; CW pump at 550 nm, $I_0 = 200 \text{ kW/cm}^2$. In the thermal simulation, the heat source is present only in the left structure. The other nano-chair acts as a temperature probe to evaluate the heat transfer. (b) Map of the temperature increase distribution for the isolated antenna with the same geometrical and excitation parameters. (c) Rescaled map of the temperature increase distribution in the probe nano-chair antenna in the dimer configuration.

3. Conclusions

In this work, we have demonstrated the beam steering of the nonlinear SH signal generated by a dielectric metastructure with AlGaAs symmetry-broken meta-units. The working principle relies on the SHG manipulation due to the meta-unit refractive index variations upon temperature changes, the latter being induced by an external CW beam. Firstly, by properly tuning the CW incident intensity, we have created a look-up table for the amplitude and the phase of the emitted SH signal from each nano-chair meta-atoms. Secondly, we have demonstrated that such look-up table can be used as a tool for tuning the SH emission. Following this approach, we have predicted a SH beam steering of 8° for the optimized device. We believe that these results may open the way to new reconfigurable metasurfaces.

Appendix

Pump polarization

The SH Far Field emission is studied as a function of the incident pump polarization, see Fig. 7. For an exciting plane wave polarized along the y axis the generated SH field present a maximum along the vertical direction while in the case of x -polarized pump beam the emitted SH has a null along the normal axes. In doing this comparison, for simplicity, the CW control signal is assumed to be co-polarized with respect the FW pump. However, we verify that no significant temperature variations in the nano-chair are observed by switching the CW polarization from being co- or cross-polarized with respect to the fundamental pump.

Supercell considerations

An array of antennas is, by definition, constituted by a finite number of identical antennas, with the same orientation, and excited in such a way that the current distributions in each antenna forming the array have the same shape but can differ in phase. It follows that the array radiation diagram is always the product of two functions, one that represents the radiation diagram of the isolated antenna and another one, usually named array factor, that can be interpreted as the shape factor of the entire system. The array factor, $F(u)$, is defined as $F(u) = \sin(nu)/\sin(u)$ with $u = (\pi/\lambda)P \cos \psi - (\delta/2)$. In the previous equation λ is the working wavelength, P the distance between each antenna, n the number of antennas, ψ the emission angle, and δ is the phase shift. In particular, a linear array is said to be broad-side if the direction of the maximum lobe of F

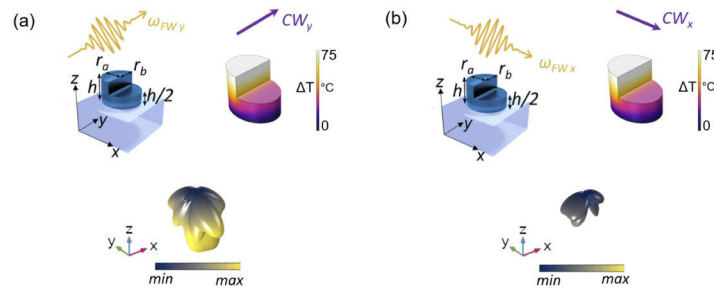


Fig. 7. The SH Far Field emission (bottom panels) when the FW light is respectively (a) y -polarized or (b) x -polarized, as sketched in the upper panels. The SH plots are drawn with the same color bar. A control CW signal equal to 200 kW/cm^2 is assumed in both cases.

is perpendicular to the alignment direction. Figure 8 shows the obtained radiation diagram for a supercell with different choice of the parameters. In particular, Fig. 8(a) represents the total radiation diagram as a function of the distance P between the nanoantennas, instead Fig. 8(b) elucidates the total emission behavior by increasing the number of resonators at fixed period.

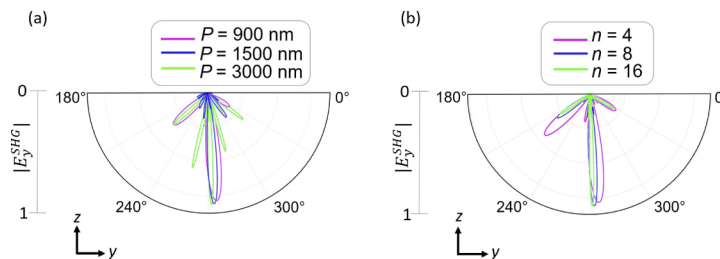


Fig. 8. The total radiation diagram as a function (a) of the metasurface period or (b) by varying the number of nano-chairs.

Thermal expansion of the nanochair

One may wonder if the temperature increase in the system is enough to generate a mechanical deformation due to the thermal expansion. Indeed, the thermally induced mechanical deformation might alter the shape of the nanochair and hinder the tunability.

In order to confute this hypothesis, we added a solid mechanics physics node in our COMSOL Multiphysics model. The temperature increase computed with the previous step is used to calculate the induced thermal strain, which is introduced as a source term for the mechanical problem [57]. The latter problem is solved with a steady-state study. The sapphire substrate is modelled as a hemisphere of radius $\sim 26 \mu\text{m}$. On the hemisphere external surface far from the nanochair, a zero-displacement (fixed) boundary condition is set. On all the other external boundaries, a zero-stress (free) boundary condition is chosen. The AlGaAs nanochair has a cubic crystalline structure, whose density is 5072 kg/m^3 [58]. The elastic constants are $C_{11} = 118.8 \text{ GPa}$, $C_{12} = 53.8 \text{ GPa}$ and $C_{44} = 59.4 \text{ GPa}$ (we used the GaAs elastic constants taken from Ref. [59] as a good approximation). The sapphire substrate has been considered homogeneous and isotropic. The density is 3980 kg/m^3 [59], the Young modulus is 300 GPa and the Poisson ratio is 0.22 [60,61].

Fig. 9 represents the deformation of the system due to the thermal expansion. The colour scale depicts the norm of the displacement field $|\mathbf{u}|$ occurring in the system. As we can see, the maximum displacement obtained for a CW beam of wavelength 550 nm and intensity

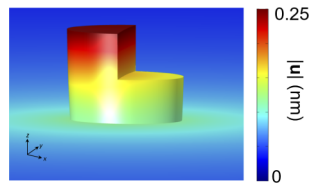


Fig. 9. Plot of the nanochair deformation due to the thermal expansion. The colour scale represents the norm of the displacement field ($|u|$). The deformation has been magnified by 200 times, for the sake of visualization. A CW beam of wavelength 550 nm and intensity 200 kW/cm² is used.

200 kW/cm² does not exceed 0.25 nm, a dimension far below the experimental uncertainty of real experiments. In view of this result, the thermal expansion does not alter the tunability performances demonstrated in this manuscript for the nanochair and hence we can safely neglect it.

Funding. Agence Nationale de la Recherche (ANR-18-CE92-0043, NANOPAIR); European Commission (899673, FETOPEN-01-2018-2019-2020); Consiglio Nazionale delle Ricerche (Joint Laboratories program, SAC.AD002.026); Ministero dell’Istruzione, dell’Università e della Ricerca (2017MP7F8F, PRIN NOMEN); Russian Foundation for Basic Research (20-32-90238); Grant of the President of the Russian Federation (2360.2020.2).

Disclosures. The authors declare no conflicts of interest.

Data availability. Data underlying the results presented in this paper are not publicly available at this time but may be obtained from the authors upon reasonable request.

References

- P.-Y. Chen, C. Argyropoulos, and A. Alù, “Enhanced nonlinearities using plasmonic nanoantennas,” *Nanophotonics* **1**(3-4), 221–233 (2012).
- F. Capasso, “The future and promise of flat optics: a personal perspective,” *Nanophotonics* **7**(6), 953–957 (2018).
- C. H. Chu, M. L. Tseng, J. Chen, P. C. Wu, Y.-H. Chen, H.-C. Wang, T.-Y. Chen, W. T. Hsieh, H. J. Wu, G. Sun, and D. P. Tsai, “Active dielectric metasurface based on phase-change medium,” *Laser Photonics Rev.* **10**(6), 986–994 (2016).
- X. Liu, K. Fan, I. V. Shadrivov, and W. J. Padilla, “Experimental realization of a terahertz all-dielectric metasurface absorber,” *Opt. Express* **25**(1), 191–201 (2017).
- K. Fan, J. Y. Suen, X. Liu, and W. J. Padilla, “All-dielectric metasurface absorbers for uncooled terahertz imaging,” *Optica* **4**(6), 601–604 (2017).
- A. I. Kuznetsov, A. E. Miroshnichenko, M. L. Brongersma, Y. S. Kivshar, and B. Luk’yanchuk, “Optically resonant dielectric nanostructures,” *Science* **354**(6314), aag2472 (2016).
- S. Kruk and Y. Kivshar, “Functional meta-optics and nanophotonics governed by mie resonances,” *ACS Photonics* **4**(11), 2638–2649 (2017).
- I. Staude, T. Pertsch, and Y. S. Kivshar, “All-dielectric resonant meta-optics lightens up,” *ACS Photonics* **6**(4), 802–814 (2019).
- N. Yu and F. Capasso, “Flat optics with designer metasurfaces,” *Nat. Mater.* **13**(2), 139–150 (2014).
- A. Arbabi, R. M. Briggs, Y. Horie, M. Bagheri, and A. Faraon, “Efficient dielectric metasurface collimating lenses for mid-infrared quantum cascade lasers,” *Opt. Express* **23**(26), 33310–33317 (2015).
- E. Arbabi, A. Arbabi, S. M. Kamali, Y. Horie, and A. Faraon, “High efficiency double-wavelength dielectric metasurface lenses with dichroic birefringent meta-atoms,” *Opt. Express* **24**(16), 18468–18477 (2016).
- Z. Wang, T. Li, A. Soman, D. Mao, T. Kananen, and T. Gu, “On-chip wavefront shaping with dielectric metasurface,” *Nat. Commun.* **10**, 1–7 (2019).
- A. Abbaszadeh, M. Ahmadi-Boroujeni, and A. Tehranian, “A compact polarization insensitive all-dielectric metasurface lens for gaussian to tophat beam shaping in sub-terahertz regime,” *Opt. Commun.* **462**, 125313 (2020).
- A. Tittl, A. Leitis, M. Liu, F. Yesilkoy, D.-Y. Choi, D. N. Neshev, Y. S. Kivshar, and H. Altug, “Imaging-based molecular barcoding with pixelated dielectric metasurfaces,” *Science* **360**(6393), 1105–1109 (2018).
- A. Tognazzi, D. Rocco, M. Gandolfi, A. Locatelli, L. Carletti, and C. De Angelis, “High quality factor silicon membrane metasurface for intensity-based refractive index sensing,” *Optics* **2**(3), 193–199 (2021).
- M. Gandolfi, A. Tognazzi, D. Rocco, C. De Angelis, and L. Carletti, “Near-unity third-harmonic circular dichroism driven by a quasibound state in the continuum in asymmetric silicon metasurfaces,” *Phys. Rev. A* **104**(2), 023524 (2021).

17. D. Rocco, M. A. Vincenti, and C. De Angelis, "Boosting second harmonic radiation from algaas nanoantennas with epsilon-near-zero materials," *Appl. Sci.* **8**(11), 2212 (2018).
18. P. Vabishchevich, A. Vaskin, S. Addamane, N. Karl, S. Liu, A. Sharma, G. Balakrishnan, J. L. Reno, G. Keeler, M. Sinclair, I. Staude, and I. Brener, "Enhanced optical nonlinearities in all-dielectric metasurfaces," in *Novel Optical Materials and Applications*, (Optical Society of America, 2019), pp. NoT3B–3.
19. C. Zou, J. Sautter, F. Setzpfandt, and I. Staude, "Resonant dielectric metasurfaces: active tuning and nonlinear effects," *J. Phys. D: Appl. Phys.* **52**(37), 373002 (2019).
20. K. Koshelev, S. Kruk, E. Melik-Gaykazyan, J.-H. Choi, A. Bogdanov, H.-G. Park, and Y. Kivshar, "Subwavelength dielectric resonators for nonlinear nanophotonics," *Science* **367**(6475), 288–292 (2020).
21. L. Carletti, K. Koshelev, C. De Angelis, and Y. Kivshar, "Giant nonlinear response at the nanoscale driven by bound states in the continuum," *Phys. Rev. Lett.* **121**(3), 033903 (2018).
22. L. Carletti, A. Locatelli, O. Stepanenko, G. Leo, and C. De Angelis, "Enhanced second-harmonic generation from magnetic resonance in algaas nanoantennas," *Opt. Express* **23**(20), 26544–26550 (2015).
23. N. I. Zheludev and Y. S. Kivshar, "From metamaterials to metadevices," *Nat. Mater.* **11**(11), 917–924 (2012).
24. A. M. Shaltout, V. M. Shalaev, and M. L. Brongersma, "Spatiotemporal light control with active metasurfaces," *Science* **364**(6441), eaat3100 (2019).
25. A. M. Shaltout, N. Kinsey, J. Kim, R. Chandrasekar, J. C. Ndukaife, A. Boltasseva, and V. M. Shalaev, "Development of optical metasurfaces: emerging concepts and new materials," *Proc. IEEE* **104**(12), 2270–2287 (2016).
26. W. J. Padilla and R. D. Averitt, "Properties of dynamical electromagnetic metamaterials," *J. Opt.* **19**(8), 084003 (2017).
27. A. Nemati, Q. Wang, M. Hong, and J. Teng, "Tunable and reconfigurable metasurfaces and metadevices," *Opto-Electron. Adv.* **1**(5), 18000901 (2018).
28. S. V. Makarov, A. S. Zalagina, M. Tajik, D. A. Zuev, M. V. Rybin, A. A. Kuchmizhak, S. Juodkazis, and Y. Kivshar, "Light-induced tuning and reconfiguration of nanophotonic structures," *Laser Photonics Rev.* **11**(5), 1700108 (2017).
29. R. Paniagua-Dominguez, S. T. Ha, and A. I. Kuznetsov, "Active and tunable nanophotonics with dielectric nanoantennas," *Proc. IEEE* **108**(5), 749–771 (2020).
30. A. Minovich, J. Farnell, D. N. Neshev, I. McKerracher, F. Karouta, J. Tian, D. A. Powell, I. V. Shadrivov, H. Hoe Tan, C. Jagadish, and Y. S. Kivshar, "Liquid crystal based nonlinear fishnet metamaterials," *Appl. Phys. Lett.* **100**(12), 121113 (2012).
31. M. Decker, C. Kremers, A. Minovich, I. Staude, A. E. Miroshnichenko, D. Chigrin, D. N. Neshev, C. Jagadish, and Y. S. Kivshar, "Electro-optical switching by liquid-crystal controlled metasurfaces," *Opt. Express* **21**(7), 8879–8885 (2013).
32. D. Rocco, L. Carletti, R. Caputo, M. Finazzi, M. Celebrano, and C. De Angelis, "Switching the second harmonic generation by a dielectric metasurface via tunable liquid crystal," *Opt. Express* **28**(8), 12037–12046 (2020).
33. C. R. de Galarreta, I. Sinev, A. M. Alexeev, P. Trofimov, K. Ladutenko, S. G.-C. Carrillo, E. Gemo, A. Baldycheva, J. Bertolotti, and C. D. Wright, "Reconfigurable multilevel control of hybrid all-dielectric phase-change metasurfaces," *Optica* **7**(5), 476–484 (2020).
34. S. Makarov, S. Kudryashov, I. Mukhin, A. Mozharov, V. Milichko, A. Krasnok, and P. Belov, "Tuning of magnetic optical response in a dielectric nanoparticle by ultrafast photoexcitation of dense electron-hole plasma," *Nano Lett.* **15**(9), 6187–6192 (2015).
35. G. P. Zograf, M. I. Petrov, D. A. Zuev, P. A. Dmitriev, V. A. Milichko, S. V. Makarov, and P. A. Belov, "Resonant nonplasmonic nanoparticles for efficient temperature-feedback optical heating," *Nano Lett.* **17**(5), 2945–2952 (2017).
36. M. Aouassa, E. Mitsai, S. Syubaev, D. Pavlov, A. Zhizhchenko, I. Jadli, L. Hassayoun, G. Zograf, S. Makarov, and A. Kuchmizhak, "Temperature-feedback direct laser reshaping of silicon nanostructures," *Appl. Phys. Lett.* **111**(24), 243103 (2017).
37. M. A. Kats, R. Blanchard, P. Genevet, Z. Yang, M. M. Qazilbash, D. Basov, S. Ramanathan, and F. Capasso, "Thermal tuning of mid-infrared plasmonic antenna arrays using a phase change material," *Opt. Lett.* **38**(3), 368–370 (2013).
38. M. Rahmani, L. Xu, A. E. Miroshnichenko, A. Komar, R. Camacho-Morales, H. Chen, Y. Zárate, S. Kruk, G. Zhang, D. N. Neshev, and Y. S. Kivshar, "Reversible thermal tuning of all-dielectric metasurfaces," *Adv. Funct. Mater.* **27**(31), 1700580 (2017).
39. K. Zangeneh Kamali, L. Xu, J. Ward, K. Wang, G. Li, A. E. Miroshnichenko, D. Neshev, and M. Rahmani, "Reversible image contrast manipulation with thermally tunable dielectric metasurfaces," *Small* **15**(15), 1805142 (2019).
40. D. Rocco, C. Gigli, L. Carletti, G. Marino, M. A. Vincenti, G. Leo, and C. De Angelis, "Vertical second harmonic generation in asymmetric dielectric nanoantennas," *IEEE Photonics J.* **12**, 1–7 (2020).
41. D. G. Baranov, S. V. Makarov, A. E. Krasnok, P. A. Belov, and A. Alù, "Tuning of near-and far-field properties of all-dielectric dimer nanoantennas via ultrafast electron-hole plasma photoexcitation," *Laser Photonics Rev.* **10**(6), 1009–1015 (2016).
42. T. Shibanuma, T. Matsui, T. Roschuk, J. Wojcik, P. Mascher, P. Albella, and S. A. Maier, "Experimental demonstration of tunable directional scattering of visible light from all-dielectric asymmetric dimers," *ACS Photonics* **4**(3), 489–494 (2017).
43. E. Khaidarov, H. Hao, R. Paniagua-Domínguez, Y. F. Yu, Y. H. Fu, V. Valuckas, S. L. K. Yap, Y. T. Toh, J. S. K. Ng, and A. I. Kuznetsov, "Asymmetric nanoantennas for ultrahigh angle broadband visible light bending," *Nano Lett.* **17**(10), 6267–6272 (2017).

44. T. Skauli, P. Kuo, K. Vodopyanov, T. Pinguet, O. Levi, L. Eyres, J. Harris, M. Fejer, B. Gerard, L. Becouarn, and E. Lallier, "Improved dispersion relations for gaas and applications to nonlinear optics," *J. Appl. Phys.* **94**(10), 6447–6455 (2003).
45. C. Gigli, G. Marino, A. Artioli, D. Rocco, C. De Angelis, J. Claudon, J.-M. Gérard, and G. Leo, "Tensorial phase control in nonlinear meta-optics," *Optica* **8**(2), 269–276 (2021).
46. S. Gehrsitz, F. Reinhart, C. Gourgon, N. Herres, A. Vonlanthen, and H. Sigg, "The refractive index of al x ga 1- x as below the band gap: accurate determination and empirical modeling," *J. Appl. Phys.* **87**(11), 7825–7837 (2000).
47. A. C. DeFranzo and B. Pazol, "Index of refraction measurement on sapphire at low temperatures and visible wavelengths," *Appl. Opt.* **32**(13), 2224–2234 (1993).
48. M. Gandolfi, C. Giannetti, and F. Banfi, "Temperonic crystal: A superlattice for temperature waves in graphene," *Phys. Rev. Lett.* **125**(26), 265901 (2020).
49. M. Celebrano, D. Rocco, M. Gandolfi, A. Zilli, F. Rusconi, A. Tognazzi, A. Mazzanti, L. Ghirardini, E. A. Pogna, L. Carletti, C. Baratto, G. Marino, C. Gigli, P. Biagioni, L. Duó, G. Cerullo, G. Leo, G. Della Valle, M. Finazzi, and C. De Angelis, "Optical tuning of dielectric nanoantennas for thermo-optically reconfigurable nonlinear metasurfaces," *Opt. Lett.* **46**(10), 2453–2456 (2021).
50. L. Carletti, D. de Ceglia, M. Vincenti, and C. De Angelis, "Self-tuning of second-harmonic generation in gaas nanowires enabled by nonlinear absorption," *Opt. Express* **27**(22), 32480–32489 (2019).
51. K. Frizyuk, "Second-harmonic generation in dielectric nanoparticles with different symmetries," *J. Opt. Soc. Am. B* **36**(8), F32–F37 (2019).
52. S. Gladyshev, K. Frizyuk, and A. Bogdanov, "Symmetry analysis and multipole classification of eigenmodes in electromagnetic resonators for engineering their optical properties," *Phys. Rev. B* **102**(7), 075103 (2020).
53. C. A. Balanis, *Antenna theory: analysis and design* (John Wiley & sons, 2015).
54. M. Dú, D. Massoubre, J. Harmand, and J. Oudar, "Thermal conductance of laterally-wet-oxidised GaAs/AlxOy Bragg reflectors," *Electron. Lett.* **42**, 1 (2006).
55. J. A. Johnson, J. K. Eliason, A. A. Maznev, T. Luo, and K. A. Nelson, "Non-diffusive thermal transport in gaas at micron length scales," *J. Appl. Phys.* **118**(15), 155104 (2015).
56. T. Luo, J. Garg, J. Shiomi, K. Esfarjani, and G. Chen, "Gallium arsenide thermal conductivity and optical phonon relaxation times from first-principles calculations," *EPL* **101**(1), 16001 (2013).
57. M. Gandolfi, F. Banfi, and C. Glorieux, "Optical wavelength dependence of photoacoustic signal of gold nanofluid," *Photoacoustics* **20**, 100199 (2020).
58. S. Adachi, "Gaas, alas, and al x ga 1- x as: Material parameters for use in research and device applications," *J. Appl. Phys.* **58**(3), R1–R29 (1985).
59. B. A. Auld, *Acoustic fields and waves in solids* (John Wiley & Sons, 1973).
60. F. Medeghini, A. Crut, M. Gandolfi, F. Rossella, P. Maioli, F. Vallée, F. Banfi, and N. Del Fatti, "Controlling the quality factor of a single acoustic nanoresonator by tuning its morphology," *Nano Lett.* **18**(8), 5159–5166 (2018).
61. A. Ronchi, A. Sterzi, M. Gandolfi, A. Belarouci, C. Giannetti, N. Del Fatti, F. Banfi, and G. Ferrini, "Discrimination of nano-objects via cluster analysis techniques applied to time-resolved thermo-acoustic microscopy," *Ultrasonics* **114**, 106403 (2021).